Chapter 4

Breakdown Characteristics of Varistor Ceramics

Jianying Li, Kangning Wu and Yuwei Huang

Additional information is available at the end of the chapter

http://dx.doi.org/10.5772/intechopen.79720

Abstract

Breakdown characteristics are of great importance for varistor ceramics, which largely depend on Schottky barriers at grain boundaries. In order to enhance breakdown performance for meeting the requirement of device miniaturization, different doping methods are introduced to not only restrict grain size from additional phase but also manipulate defect structure of Schottky barrier at grain boundaries from substitution. Distribution of barriers is another key point affecting breakdown characteristics in varistor ceramics. Dimensional effect, which is detected in not only ZnO ceramics but also $CaCu_3Ti_4O_{12}$ ceramics, is practically and theoretically found to be closely correlated with uniformity of grains. As a result, breakdown characteristics of varistors are dominated by combination effect of single barrier performance and spatial barrier distribution. In this chapter, enhanced breakdown field in $Ca_xSr_{1-x}Cu_3Ti_4O_{12}$ ceramics, in situ synthesized $CaCu_3Ti_4O_{12}$-$CuAl_2O_4$ ceramics, and $CaCu_3Ti_4O_{12}$-$Y_{2/3}Cu_3Ti_4O_{12}$ composite ceramics are investigated from the aspect of Schottky barriers at grain boundaries. In addition, dimensional effect is found in both ZnO and $CaCu_3Ti_4O_{12}$ ceramics, which are investigated from grain size distribution through theoretical and experimental analysis.

Keywords: breakdown characteristics, varistor ceramics, Schottky barrier, $CaCu_3Ti_4O_{12}$ ceramics, ZnO ceramics

1. Introduction

Varistor ceramics exhibit excellent nonlinear current-voltage (*I-V*) characteristics that they are widely employed for overvoltage protection in power system and electronic circuits. Zinc oxide (ZnO) varistor ceramics is one typical varistor ceramics, which has been for decades widely employed in arrestors [1]. The breakdown field of commercial ZnO varistor ceramics is commonly 200–300 V/mm and the nonlinear coefficient is ~50. Besides, perovskite $CaCu_3Ti_4O_{12}$ (CCTO) ceramics exhibit giant permittivity and nonlinear characteristics that

made them potential candidates for application in surge absorption [2, 3]. Varistor ceramics consist of grains and grain boundaries, and it is grain boundary which manipulates the breakdown field. Breakdown field is commonly suggested to be dominated by single grain boundary and the amount of grain boundaries along electric field direction. The single grain boundary electrical performance is determined by Schottky barriers which are primarily comprised of positively charged depletion layers and negatively charged interface states [4]. Meanwhile, the amount of grain boundaries is decided by grain size. With the progress of device miniaturization, the demand for varistor ceramics with high breakdown field and high-energy absorption capability needs to be fulfilled. In order to enhance breakdown characteristics, microstructure of varistor ceramics should be improved which can be summarized into decreasing grain sizes on one hand and enhancing single barrier performance on the other hand. Two major ways of achieving greater breakdown characteristics are (1) improving preparation method and (2) finding a better recipe which might contain additives [5–10]. For improved preparation process, lots of methods like nano-sized particles and spark plasma sintering (SPS) techniques are induced to reduce the grain sizes [11, 12]. Doping is another typical topic in enhancing breakdown performance in varistor ceramics. As is known in ZnO varistor ceramics, nonlinear properties do not exist until Bi_2O_3 is added which forms an intergranular layer and manipulates defect structure to form better Schottky barriers at grain boundaries. Later on, Sb_2O_3, Co_2O_3, Mn_2O_3, etc. are added to further enhance breakdown field and improve nonlinear performance. As for CCTO varistor ceramics, several doping methods were introduced which have different effects on microstructure. Firstly, the doping ions are able to substitute ions in CCTO lattice (Ca^{2+}, Cu^{2+}) and form a relatively homogeneous structure [5]. This method dominantly manipulates Schottky barrier structure at grain boundaries. Secondly, another phase is formed besides CCTO phase resulting in heterogeneous structure, like $SrTiO_3$, TiO_2, $CuAl_2O_4$, etc. [6–8]. The additional phases mainly restrict the growth of grains and control the grain size to produce more grain boundaries. Thirdly, to form another CCTO-like phase with CCTO phase, like $Y_{2/3}Cu_3Ti_4O_{12}$ [9], is also suggested. This method not only introduces heterogeneous structure which restricts grain growth but also induces more defects at grain boundaries to enhance Schottky barriers. In summary, these three methods of doping result in diverse improvement of electrical characteristics due to various effects on microstructure of varistor ceramics. In the main text, these three kinds of doping methods are, respectively, introduced in detail.

Besides methods of enhancing breakdown characteristics, a non-negligible phenomenon that electrical performance is not uniform in the bulk of the ceramics should be taken into consideration for design and practical application. The inhomogeneous electrical properties at the cross section have been widely reported. About 5–11% of cross-section region in varistor ceramics was found to exhibit lower breakdown voltage than the rest of the regions [13]. This further results in current localization, which causes electrical puncture, thermal cracking, or even thermal runaway [14]. In addition, dimensional effect, which exhibits as the thickness dependence of breakdown field, is found in not only ZnO ceramics but also CCTO ceramics [15–17]. It is found that breakdown field and nonlinear coefficient are significantly decreased below a critical thickness, which brings much trouble in designing. The spatial electrical nonuniformity was widely attributed to inhomogeneous grain size distribution and grain

boundary characteristics. Electrical measurements using microcontact on single grain boundary suggested that 50% grain boundaries can be defined as "good," 30% are "bad," and the rest are ineffective [18]. At the same time, reports from luminescence created by electrical breakdown also provide support for uneven grain boundaries [19]. In this work, the structural origin of dimensional effect in varistor ceramics is investigated through experiment and simulation, which suggested that wide grain size distribution should be responsible. After careful processing of controlling grain sizes into narrower distribution, dimensional effect is diminished, which, to some extent, proves the responsibility of grain size distribution.

2. Enhancement of electrical breakdown field in varistor ceramics

2.1. Enhanced breakdown field in $Ca_{1-x}Sr_xCu_3Ti_4O_{12}$ ceramics via tailoring donor density

2.1.1. Phase composition and surface morphology

X-ray diffraction (XRD) patterns of $Ca_{1-x}Sr_xCu_3Ti_4O_{12}$ ceramics are presented in **Figure 1**. Main perovskite phase of CCTO is detected with small amount of impurity phase of CuO and $SrTiO_3$ in **Figure 1(a)**. In the enlarged view of (220) peak in **Figure 1(b)**, the peak gradually moves to a lower angle with the increase of Sr/Ca ratio, indicating increased lattice constant as a result of Ca^{2+} (0.99 Å) with smaller radius being substituted by Sr^{2+} (1.26 Å).

SEM images and corresponding grain size distribution are shown in **Figure 2**. Grain size of the samples is smaller than that in CCTO ceramics (>8 μm), while it changes little on the ratio of Sr/Ca (2.4–2.8 μm). Energy dispersive X-ray spectroscopy (EDS) is further measured at the marked regions in **Figure 2** with the results listed in **Table 1**. No pure $CaCu_3Ti_4O_{12}$ or $SrCu_3Ti_4O_{12}$ is detected, indicating solid solution systems. Major discrepancy for those large

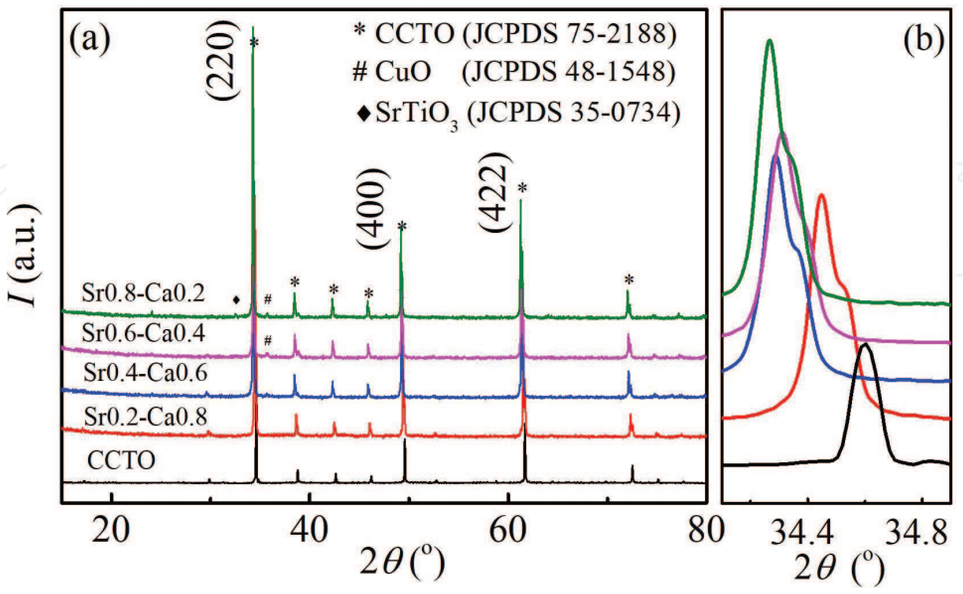

Figure 1. XRD patterns of $Ca_{1-x}Sr_xCu_3Ti_4O_{12}$ varistor ceramics.

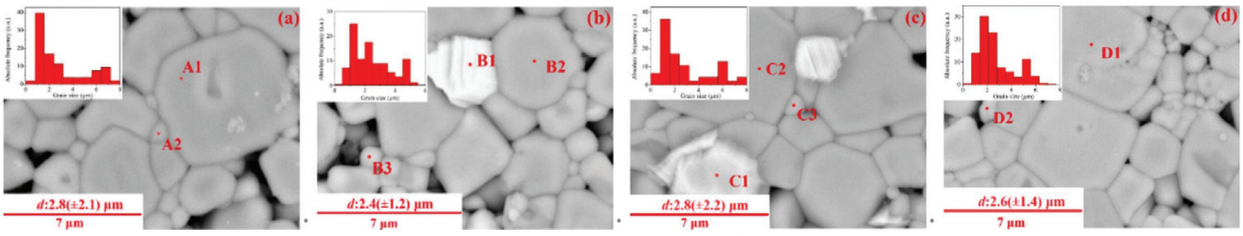

Figure 2. Backscattering SEM pictures of $Ca_{1-x}Sr_xCu_3Ti_4O_{12}$ ceramic samples. (a) Sr0.2-Ca0.8, (b) Sr0.4-Ca0.6, (c) Sr0.6-Ca0.4 and (d) Sr0.8-Ca0.2. (usage permitted by Elsevier).

Atom (%)	Sr0.2-Ca0.8		Sr0.4-Ca0.6			Sr0.6-Ca0.4			Sr0.8-Ca0.2	
	A1	A2	B1	B2	B3	C1	C2	C3	D1	D2
O K	66.68	70.31	62.31	68.99	72.75	59.20	65.93	63.45	67.67	73.60
Ti K	17.14	15.49	0.86	16.20	14.22	6.70	17.11	18.65	16.66	13.73
Cu K	11.94	10.64	36.82	10.74	9.44	32.87	12.70	13.80	11.51	9.50
Sr L	0.85	0.28		1.69	1.14	0.88	3.33	3.15	3.26	2.40
Ca K	3.39	3.27		0.71	0.46		3.54	3.31	3.66	3.08

Table 1. EDS results for marked points in **Figure 2** (usage permitted by Elsevier).

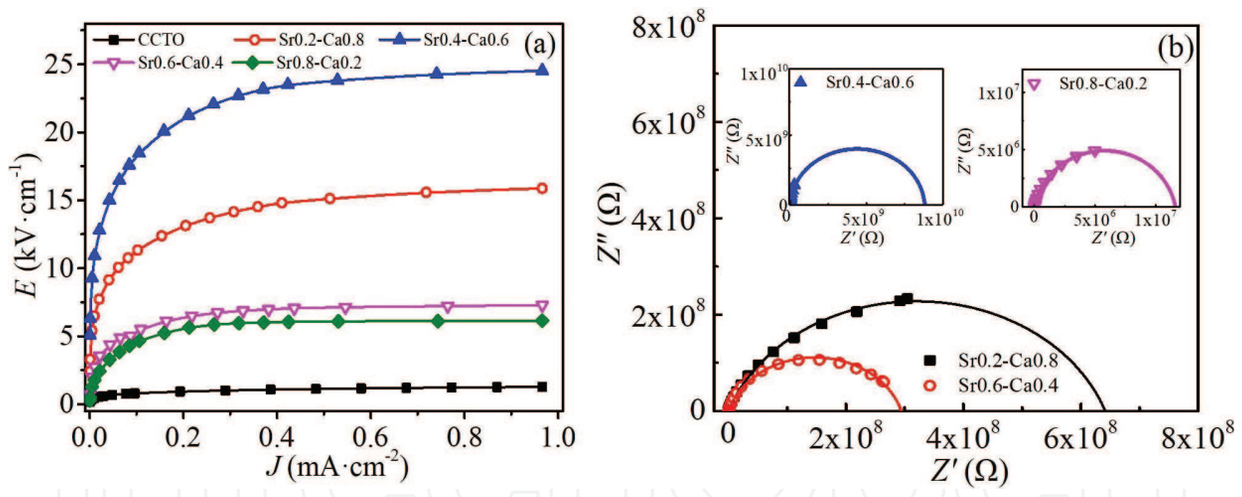

Figure 3. Current-voltage (*J-E*) characteristics (a) and impedance spectra (b) of $Ca_{1-x}Sr_xCu_3Ti_4O_{12}$ ceramics at room temperature.

grains (A1, B2, C2, D1) and small grains (A2, B3, C3, D2) is found to be Sr/Ca ratio. The higher Sr/Ca ratio in larger grains indicates Sr^{2+} might have benefit for grain growth in relatively low temperatures.

2.1.2. Enhanced breakdown field and complex impedance spectra

Figure 3 is current density-electric field (*J-E*) curves of $Ca_{1-x}Sr_xCu_3Ti_4O_{12}$ ceramics. The breakdown field E_{1mA} and nonlinear coefficient α are calculated:

$$E_{1mA} = U_{1mA}/d, \tag{1}$$

$$\alpha = \frac{1}{\log(U_{1mA}/U_{0.1mA})}, \tag{2}$$

where U_{1mA} and $U_{0.1mA}$ are the voltage under current density of 1 and 0.1 mA/cm^2, respectively, and d is the sample thickness. The corresponding α and E_{1mA} are listed in **Table 2**. Enhanced E_{1mA} are observed in $Ca_{1-x}Sr_xCu_3Ti_4O_{12}$ especially for samples with Sr/Ca ratio of 0.4/0.6. It increased remarkably to 24.52 kV/cm, which is as twice as that of CCTO. Elevated E_{1mA} can be partially ascribed to decreased grain size. However, greatly varied E_{1mA} are found in samples with similar grain size of ~2.5 μm in **Figure 2**, indicating grain size is not decisive. Series connected *RC* units are widely employed for characterizing properties of grains and grain boundaries based on the fact that CCTO ceramics consist semiconducting grains and insulating grain boundaries [2, 20]. The complex impedance *Z** can be expressed as:

$$Z^* = Z' - iZ'' = \frac{R_{gb}}{1 + i\omega R_{gb}C_{gb}} + \frac{R_g}{1 + i\omega R_g C_g}, \tag{3}$$

where R_{gb} and C_{gb} are resistance and capacitance of grain boundaries while R_g and C_g are resistance and capacitance of grains. R_g and R_{gb} can be thus obtained as intercepts in complex impedance spectra in **Figure 4**. In addition, resistance activation energies of grain (E_g) and grain boundary (E_{gb}) are calculated via the Arrhenius equation. As shown in **Table 2**, R_g and E_g remain constant to ~225 Ω and ~0.13 eV, while R_{gb} and E_{gb} vary significantly. Highest R_{gb} and E_{gb} of 9900 MΩ and 1.03 eV are obtained for samples with Sr/Ca ratio of 0.4/4.6, which is in accordance with breakdown field in **Figure 3(a)**. Consequently, it is reasonable to deduce that modified grain boundary characteristics that are crucial for the improved breakdown field.

2.1.3. Tailoring of donor density

Back-to-back Schottky barrier at grain boundary is crucial for the nonlinearity of varistors. Generally, the barrier height ϕ_0 depends on the depletion layer width x_d, interface state density N_s, and donor concentration N_d:

Samples	Sr0.2-Ca0.8	Sr0.4-Ca0.6	Sr0.6-Ca0.4	Sr0.8-Ca0.2
α	6.83	8.11	8.24	8.32
E_{1mA} (kV/cm)	15.88	24.52	7.28	6.15
R_g (Ω)	221	221	234	233
R_{gb} (MΩ)	640	9900	270	12
E_g (eV)	0.14	0.13	0.14	0.13
E_{gb} (eV)	1.01	1.03	0.86	0.71

Table 2. Parameters for electrical nonlinearity and inhomogeneity of grain and grain boundary of $Ca_{1-x}Sr_xCu_3Ti_4O_{12}$ varistor ceramics.

$$\phi_0 = \frac{eN_s^2}{8\varepsilon_0\varepsilon_r N_d}. \tag{4}$$

For single grain boundary, the grain boundary capacitance of unit area C_0 under zero biased voltage is $C_0 = [e\varepsilon_r N_d/(8\phi_0)]^{1/2}$, while the capacitance C under a bias voltage U is as follows [21]:

$$\left(\frac{1}{C} - \frac{1}{2C_0}\right)^2 = \frac{2(\phi_0 + U)}{e\varepsilon_r N_d}. \tag{5}$$

Dependence of $(C^{-1} - 1/2C_0{}^{-1})$ on U is plotted in **Figure 4**, showing good nonlinearity. Barrier parameter is calculated and listed in **Table 3**. N_d for all the samples is almost constant, while N_s varies remarkably from 3.3×10^{13} cm^{-3} for Sr0.4-Ca0.6 to 15.6×10^{13} cm^{-3} for Sr0.8-Ca0.2. Consequently, the highest barrier height is obtained in Sr0.4-Ca0.6 and lowest in Sr0.8-Ca0.2, which matches the results of E_{gb} from impedance spectra.

Oxygen vacancy is considered as origin of electron formation due to weak cation—O bonds. Space of A site in CCTO is rather rigid as the observed Ca—O distance is 2.61 Å, while the

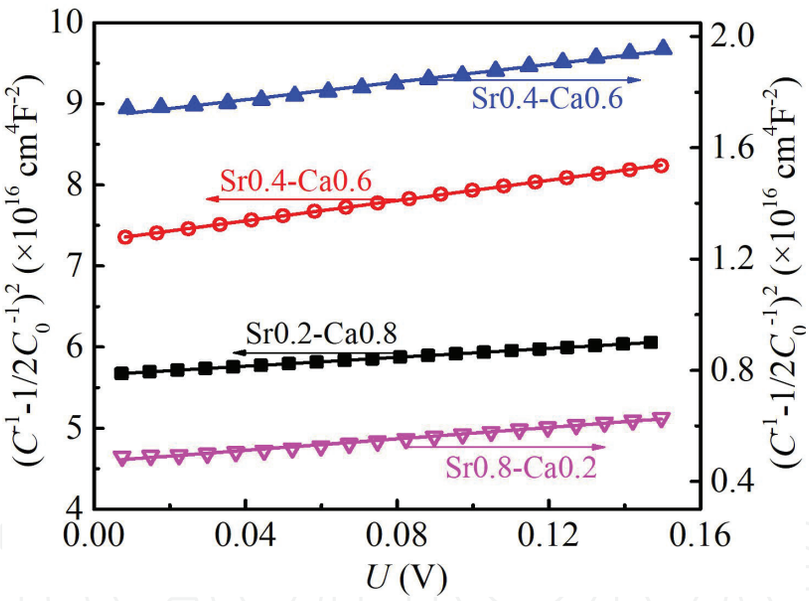

Figure 4. *C-V* characteristics of $Ca_{1-x}Sr_xCu_3Ti_4O_{12}$ varistor ceramics.

Samples	Sr0.2-Ca0.8	Sr0.4-Ca0.6	Sr0.6-Ca0.4	Sr0.8-Ca0.2
ϕ_0 (eV)	1.11	1.17	0.96	0.40
x_d (nm)	630	880	460	240
N_s (10^9 cm^{-2})	7.73	5.90	9.20	7.53
N_d (10^{13} cm^{-3})	6.11	3.34	9.99	15.67

Table 3. Parameters of Schottky barrier of $Ca_{1-x}Sr_xCu_3Ti_4O_{12}$ varistor ceramics (usage permitted by Elsevier).

expected value is 2.72 Å [22]. Radius of Sr is much larger than that of Ca so that Sr—O bonds are extremely over bonded. In increasing the ratio of Sr/Ca, larger Sr stretches the Ti—O bonds, leading to enhanced polarizability of the tilted TiO_6 octahedra and possible breaking of the balance of Cu—O plane. Therefore, oxygen vacancy is much easier to be produced as well as segregated Cu-rich secondary phase, shown in **Figure 1** [23].

On the contrary, oxygen vacancy may be inhibited due to solid solution effect between SCTO and CCTO. Taking Sr^{2+} in CCTO as an example, besides Sr_{Ca}, Sr exists as Sr_{Cu} and $Sr_i^{\cdot\cdot}$ as Cu^{2+} is easily loss in CCTO. Sr-Cu distortion is likely formed due to the same valence of Sr, Ca, and Cu ions. Increased *A* site ions can coordinate with the O^{2-} in TiO_6 octahedron. Moreover, $Sr_i^{\cdot\cdot}$ can compensate the electrons generated by oxygen vacancies. As a result, declined donor density is thus formed, which can result from Ca in SCTO as well. Maximum integrated action of strong solid solution effect and weak Sr stretching effect is achieved when Sr/Ca ratio is 40/60, which leads to greatly elevated potential barrier height more than 1.0 eV and enhanced breakdown field consequently.

2.2. In situ synthesized CCTO-xCuAl$_2$O$_4$ varistor ceramics

2.2.1. Preparation and characterization of in situ synthesized CCTO-x$CuAl_2O_4$ samples

CCTO powders are prepared via traditional solid-state reaction method and suspended in $Al(NO_3)_3$ aqueous solution. Subsequently, the suspension was quantitatively titrated with NH_4OH to make $Al(OH)_3$ precipitate on the surface of CCTO particles. After drying, the powders are calcined at 950°C for 4 h to dehydrate $Al(OH)_3$ into Al_2O_3. Finally, they were pressed into pellets and sintered in air at 1100°C for 4 h.

XRD patterns are presented in **Figure 5(a)**. Only single phase of CCTO can be detected when $x = 0$. With increased precipitation of Al^{3+}, another spinel phase $CuAl_2O_4$ is found. Backscattering

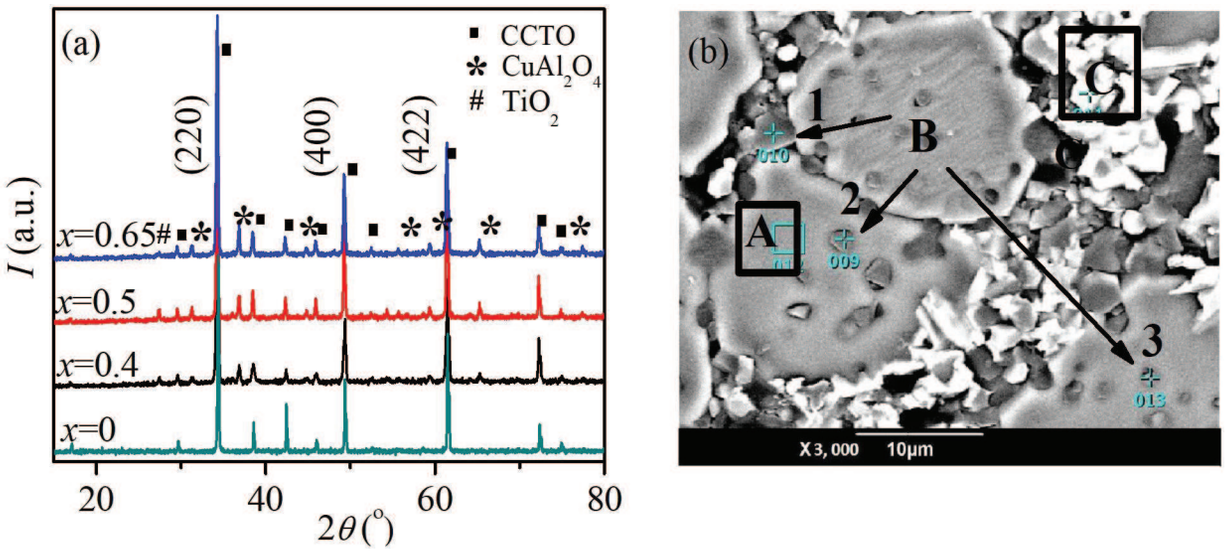

Figure 5. XRD patterns (a) and SEM picture (b) of in situ synthesized CCTO-xCuAl$_2$O$_4$ ceramics (usage permitted by IOP Publishing).

SEM picture of CCTO-0.4$CuAl_2O_4$ sample is further taken as shown in **Figure 5(b)**, in which three typical regions, A, B, and C, can be observed. According to EDS results presented in **Table 4**, element distribution of the gray grains (A, 15–20 μm in size) is similar to CCTO with a little Al. The black grains (B1, B2, and B3, 1–4 μm in size) are found to be the secondary phase, while the bright region of C is Cu-rich intergranular phase. It is proposed that Cu_2O and CuO are easily precipitated over 1000°C as Cu-rich phase, which is the main source for $CuAl_2O_4$. The involved chemical reactions can be expressed as:

$$\begin{aligned} 2Al(OH)_3 &= Al_2O_3 + 3H_2O\uparrow \\ CuO + Al_2O_3 &= CuAl_2O_4 \\ Cu_2O + 2Al_2O_3 + \frac{1}{2}O_2 &= 2CuAl_2O_4. \end{aligned} \tag{6}$$

Surface morphology of the samples is characterized by SEM as shown in **Figure 6**. For CCTO ceramics, little secondary phase is found, and the average grain size is 19.1 μm as shown in **Figure 6(a)**. As to samples with $x = 0.4$ found in **Figure 6(b)**, numbers of small particles appear in interior and intergranular region of CCTO grains, and the average grain size is 18.8 μm. When x increases to 0.5 and 0.65, average grain sizes decrease notably to about 1.6 μm. It is proposed that reduction of grain size may arise from the depleted Cu-rich phases, which assists grain growth in forming $CuAl_2O_4$ according to Eq. (4). Pinning effect of $CuAl_2O_4$ phase could further inhibit the grain growth, which generally obeys the Zener model:

Atom (%)	A	B1	B2	B3	C
O K	41.97	39.6	44.64	50.37	37.81
Al K	1.42	41.55	28.38	19.70	0.79
Ca K	6.56	0.61	2.26	3.12	1.10
Ti K	28.81	2.60	9.35	12.44	5.17
Cu K	21.25	15.63	15.37	14.37	55.13

Table 4. EDS results of in situ synthesized CCTO-0.4$CuAl_2O_4$ sample in **Figure 5(b)** (usage permitted by IOP Publishing).

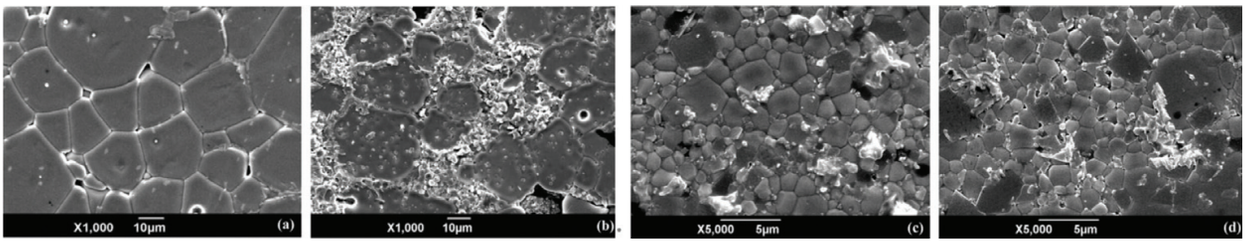

Figure 6. SEM images of CCTO-$x$$CuAl_2O_4$ ceramic samples: (a) $x = 0$, (b) $x = 0.4$, (c) $x = 0.5$, and (d) $x = 0.65$ (usage permitted by Elsevier).

$$\frac{G}{r} = \frac{4}{3} f^{-1}, \tag{7}$$

where G is the limit size of the matrix grain and r and f are particle diameter and volume fraction of the secondary phase, respectively. The grain size of the secondary phase decreases, and the volume fraction of the secondary phase increases; the matrix grain size apparently declines. Therefore, the best pining effect is achieved in the sample with $x = 0.5$ for relatively small grain size and high volume fraction of the spinel phase.

2.2.2. Enhanced breakdown field in CCTO-x$CuAl_2O_4$ ceramic samples

J-E characteristics of in situ synthesized CCTO-$x$$CuAl_2O_4$ ceramics are plotted in **Figure 7**, and the corresponding E_{1mA} and α are plotted in the inset. It is clear that E_{1mA} of samples with $x = 0.5$ increased sharply to about 21 kV/cm with reduced grain size. On this basis, it is proposed that aggregation of $CuAl_2O_4$ and the inhibiting of grain growth should take responsibility for the greatly enhanced E_{1mA}. Although $E_{1mA} = 4.3$ kV/cm is found in $x = 0.65$ samples with similar grain size of ~1.6 μm, it can be ascribed to abnormally large grains as presented in **Figure 6(d)**.

For comparison, $CuAl_2O_4$ is directly introduced into CCTO by solid-state reaction method following the same sintering condition. Dependence of α and E_{1mA} on addition of the secondary phase is plotted in **Figure 7(b)**. Similar to the in situ synthesized samples, the highest E_{1mA} is achieved when $x = 0.5$. However, its highest E_{1mA} is only about 15 kV/cm. This suggests that enhanced E_{1mA} in directly induced samples mainly arise from pinning effect while additional depletion of Cu-rich phase should be also considered for in situ synthesized samples.

2.2.3. Complex impedance analysis for CCTO-x$CuAl_2O_4$ samples

Figure 8(a) is complex impedance spectra of CCTO-$x$$CuAl_2O_4$ samples at 393 K. R_{gb} increases greatly from 0.37 to 13.55 MΩ with increased Al. Based on the dominant effect of R_{gb} to the overall resistance, DC conductivity can approximate to conductivity of grain boundary. Activation energy of DC conductivity can be thus calculated via the Arrhenius equation, as shown

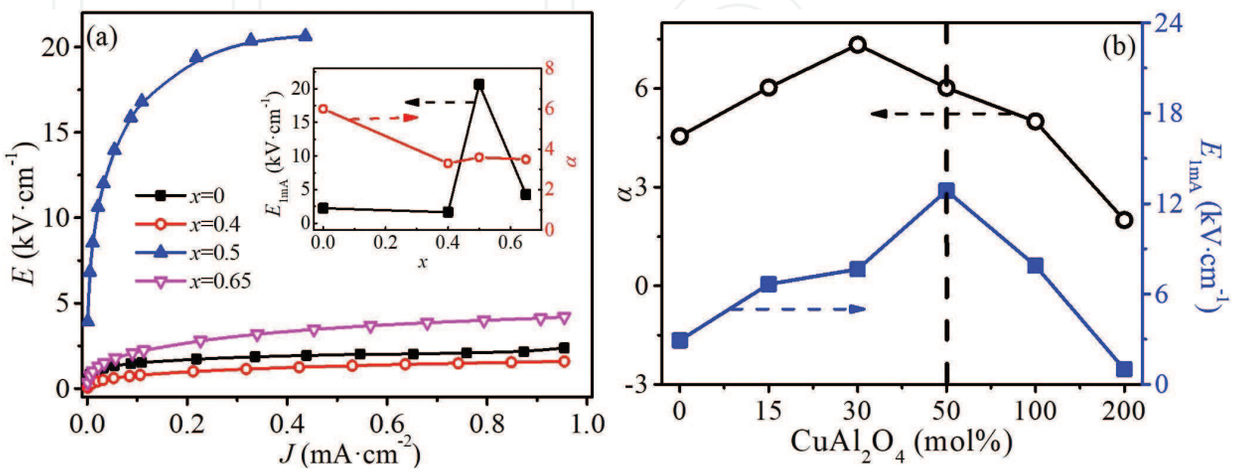

Figure 7. *J-E* characteristics of in situ synthesized (a) and directly induced (b) CCTO-$x$$CuAl_2O_4$ samples.

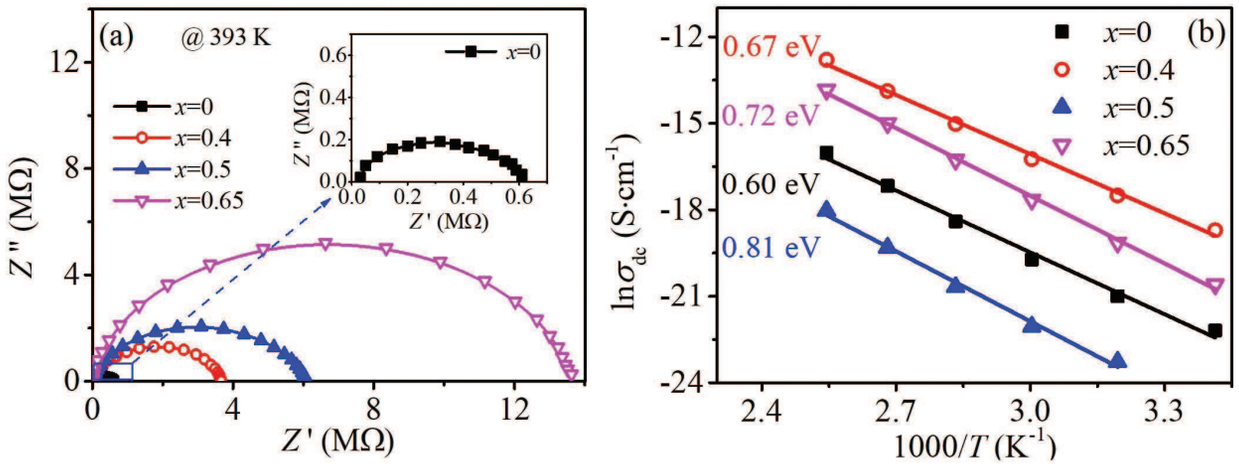

Figure 8. Impedance spectra (a) and temperature dependence of DC conductivity (b) of CCTO-xCuAl$_2$O$_4$.

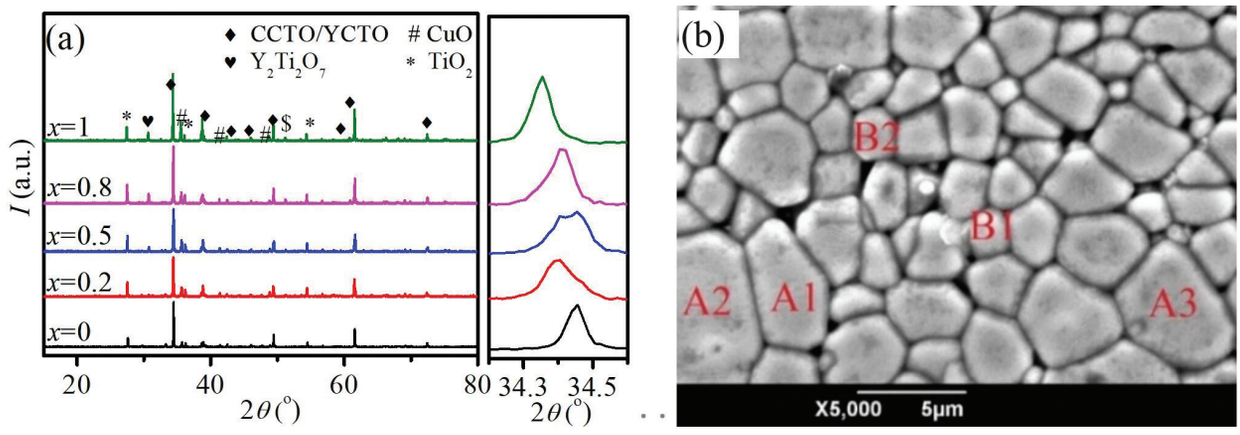

Figure 9. XRD patterns (a) and SEM picture (b) of 0.2CCTO-0.8YCTO ceramics (usage permitted by Elsevier).

in **Figure 8(b)**. Highest energy of 0.81 eV is found for samples with x = 0.5, indicating inhibited hopping conduction process in them. Thus, it is suggested that the new formation of insulating phase $CuAl_2O_4$ may modify the electronic structure of grain boundaries and improve the electrical properties of CCTO ceramics. The enhanced R_{gb} can be attributed to higher activation energy required for hopping conduction at grain boundary.

2.3. CCTO-YCTO composite ceramics with enhanced nonlinearity

2.3.1. Phase composition and surface morphology

$(1 - x)CaCu_3T_4O_{12}$-$xY_{2/3}Cu_3T_4O_{12}$ [$(1 - x)$CCTO-xYCTO] ceramics were prepared via solid-state reaction method. They were sintered in air at 1100°C for 10 h. XRD patterns are shown in **Figure 9(a)**, in which the main phase of perovskite phase and small amount of CuO, TiO_2, and $Y_2Ti_2O_7$ are detected. With increased Y^{3+}, (200) peak moves to lower angle. However, it is hard to identify CCTO with YCTO phase due to similar lattice structure. Therefore, EDS is conducted (**Figure 9(b)** and **Table 5**). Element distribution of the large gains (4–6 μm) is close to YCTO, while small grains (1–2 μm) are close to CCTO although solid solution is found.

Atom (%)	A1	A2	A3	B1	B2
Y K	4.00	4.6	4.56	0.89	0.85
Ca K	0.87	0.61	0.94	4.90	4.76
Cu K	9.08	8.29	7.98	9.15	10.34
Ti K	20.49	19.41	19.89	20.77	21.77
O K	64.86	66.09	65.62	64.29	61.89

Table 5. EDS results of 0.2CCTO-0.8YCTO sample in **Figure 9(b)** (usage permitted by Elsevier).

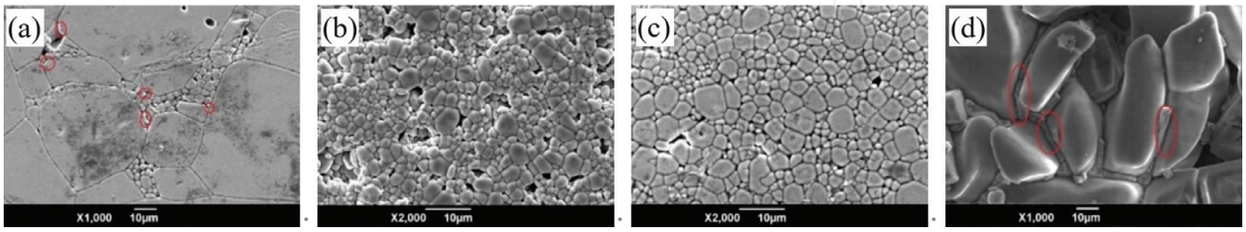

Figure 10. Surface morphology of $(1 - x)$CCTO-xYCTO ceramics: (a) $x = 0$, (b) $x = 0.5$, (c) $x = 0.8$, and (d) $x = 1.0$.

SEM pictures were taken, as shown in **Figure 9**. Large grains are formed in pure CCTO and YCTO ceramics with Cu-rich phase segregated in the intergranular region marked by red circles as shown in **Figure 10(a)** and **(d)**. Discontinuous distribution of grain size is finally formed in CCTO samples. Stripy grains in pure YCTO ceramics suggest that sintering temperature is so high that grains could not hold the hexagonal shape. Meanwhile, two kinds of grains, with grain sizes of 4–6 μm and 1–2 μm, respectively, were found uniformly distributed in composite ceramics. Average grain size is reduced, which indicates that grain growth of CCTO and YCTO was suppressed by each other in the form of pinning effect.

2.3.2. Enhanced electrical nonlinearity

J-E characteristics at room temperature are presented in **Figure 11**. E_{1mA} of 0.5CCTO-0.5YCTO and 0.2CCTO-0.8YCTO are enhanced to 10.17 and 11.24 kV/cm, respectively, which are approximately 10 times of that 1.24 kV/cm of CCTO sample. α is improved to 9.57 and 9.88, respectively, as well. Although extremely high α is reported in some reports, they are hard to be repeated. α largely depends on the current range used for calculation in Eq. (2) and the measuring method. As shown in **Figure 11(b)**, some reports of high α are actually ~5 in the current range 0.1–1 mA/cm in ln*J*–ln*E* plots [24–26]. The reported high α might also originate from positive feedback of heat generated from thermal emission process at grain boundary.

Complex impendence spectroscopy at room temperature is plotted in **Figure 12**. R_g is close to 20–40 Ω, and R_{gb} varies significantly up to 1200 MΩ in samples with $x = 0.8$, while it is 55.5 MΩ in pure CCTO. To further explore the carriers' migration across barrier, E_g and E_{gb} are calculated in **Table 6**. Similar to other reports, E_g is constant while E_{gb} differs significantly, inferring crucial role of grain boundary on carrier transport. E_{gb} gradually increases with increased x, suggesting gradually developed Schottky barrier with the addition of YCTO. The barrier

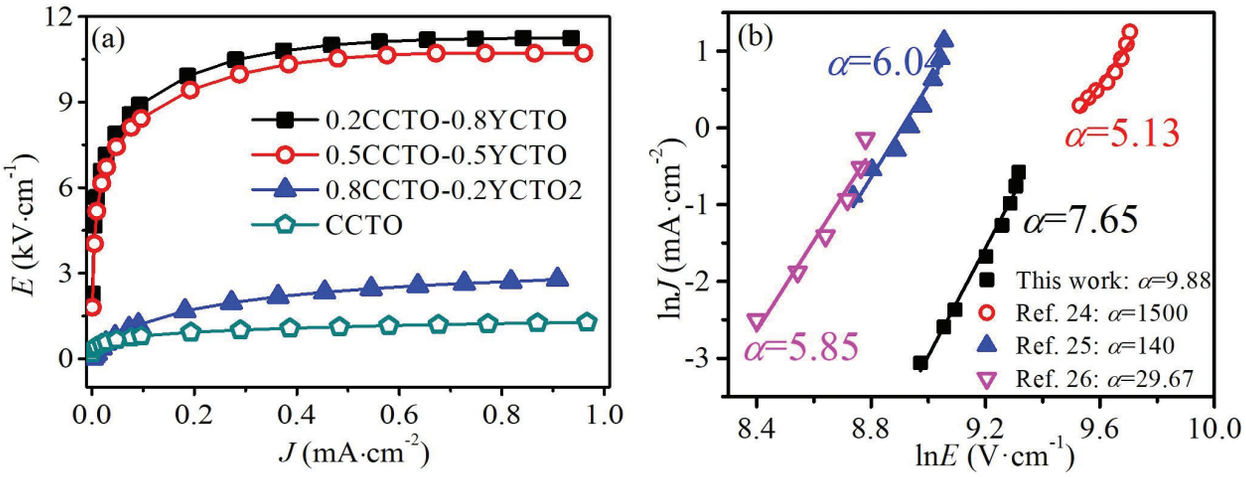

Figure 11. *J-E* characteristics of (1 − x)CCTO-*x*YCTO ceramics (a) and some reported CCTO ceramics with high nonlinear coefficient (b).

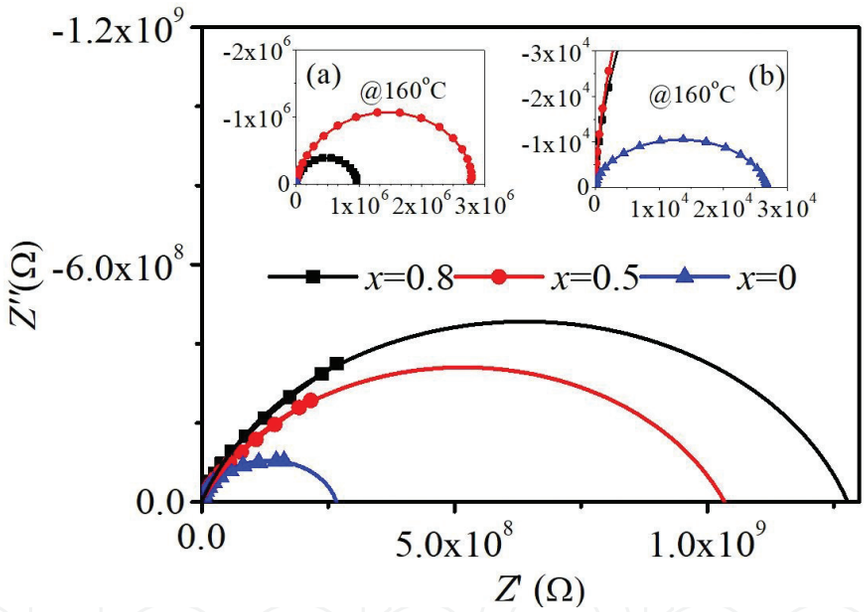

Figure 12. Complex impedance spectra of (1 − x)CCTO-*x*YCTO ceramics.

Energies	CCTO	0.5CCTO-0.5YCTO	0.8CCTO-0.2YCTO	YCTO
E_g (eV)	0.10	0.09	0.09	0.08
E_{gb} (eV)	0.69	1.11	1.50	031

Table 6. Activation energies of grain and grain boundary resistance of (1 − *x*)CCTO-*x*YCTO samples.

height of sample with $x = 0.8$ reaches a maximum of 1.50 eV, which is twice higher than 0.69 eV of CCTO. The high barrier height leads to high nonlinear coefficient, which is consistent with results of *J-E* performance shown in **Figure 11(a)**.

Grain boundary resistance dominates the conduction process. So the hopping conduction is deduced, inhibiting improved grain boundary resistance and activation energy in composite ceramics. This inhibition may arise from increased number of grain boundaries or enhanced blocking effect of single barrier. There are three types of grain boundaries: CCTO/YCTO, CCTO/CCTO, and YCTO/YCTO. E_{gb} of 0.2CCTO-0.8YCTO samples (1.43 eV) is higher than that 1.11 eV of 0.5CCTO-0.5YCTO samples, indicating effect of grain boundary type is more important. Assuming both CCTO and YCTO grains are cubic, its surface area ratio can be simply written as:

$$\frac{A_{\mathrm{CCTO}}}{A_{\mathrm{YCTO}}} = \frac{r_{\mathrm{CCTO}}^2 \times (\mathrm{Vol\%_{CCTO}}/\mathrm{Vol_{CCTO}})}{r_{\mathrm{YCTO}}^2 \times (\mathrm{Vol\%_{YCTO}}/\mathrm{Vol_{YCTO}})} = \frac{r_{\mathrm{YCTO}} \times \mathrm{Vol\%_{CCTO}}}{r_{\mathrm{CCTO}} \times \mathrm{Vol\%_{YCTO}}}, \tag{8}$$

where A is surface area of grains, r is grain size, Vol is single grain volume, and Vol% is volume fraction. Densities of CCTO and YCTO are 5.05 and 5.20 g/cm^3, respectively. The average grain sizes for CCTO and YCTO are 1.24 and 4.57 μm according to results found in **Figure 10(b** and **c)**. On this basis, it can be obtained that $A_{\mathrm{CCTO}}/A_{\mathrm{YCTO}}$ for 0.5CCTO-0.5YCTO is 0.38, while it is 0.95 for 0.2CCTO-0.8YCTO. In other words, the number of CCTO/YCTO interfaces reaches maximum in 0.2CCTO-0.8YCTO sample. On one hand, solid solution between Y^{3+} and Ca^{2+} could inhibit generation of donors, leading to thicker depletion layers. On the other hand, more interface states are produced at the YCTO/CCTO heterojunction. As a result, barrier height is improved so that more energy is needed for carriers to migrate across barriers.

3. Dimensional effect of varistor ceramics

3.1. Phenomenon of dimensional effect

Thickness dependence of $E_{1\mathrm{mA}}$ and α of ZnO ceramics with low, medium, and high potential gradients is plotted in **Figure 13(a)**. Similar phenomenon is also found in CCTO ceramics in **Figure 13(b)**. Every curve exhibits a turning point corresponding to sample thickness d. Critical thickness d_c, critical breakdown field E_c, and critical nonlinear coefficient α_c are determined by each curve. Such behavior can be empirically represented as:

$$E_{1\mathrm{mA}} \propto e^{bd}, \tag{9}$$

where the exponent b represents the transitional behavior for the entire curve. Let this exponent in $d < d_c$ domain be denoted as b_1 while it is denoted as b_2 in the $d > d_c$ domain, i.e.:

$$\ln E_{1\mathrm{mA}} = a_1 + b_1 d \ (d < d_c), \tag{10}$$

$$\ln E_{1\mathrm{mA}} = a_2 + b_2 d \ (d > d_c). \tag{11}$$

The summary of the parameters b_1, b_2, d_c, and E_c in **Figure 13** is listed in **Table 7**. d_c significantly decreases with increased $E_{1\mathrm{mA}}$ and E_c, which indicate that those who exhibit higher $E_{1\mathrm{mA}}$ exhibit less severe dimensional effect. At the same time, b_2 slightly decreases with

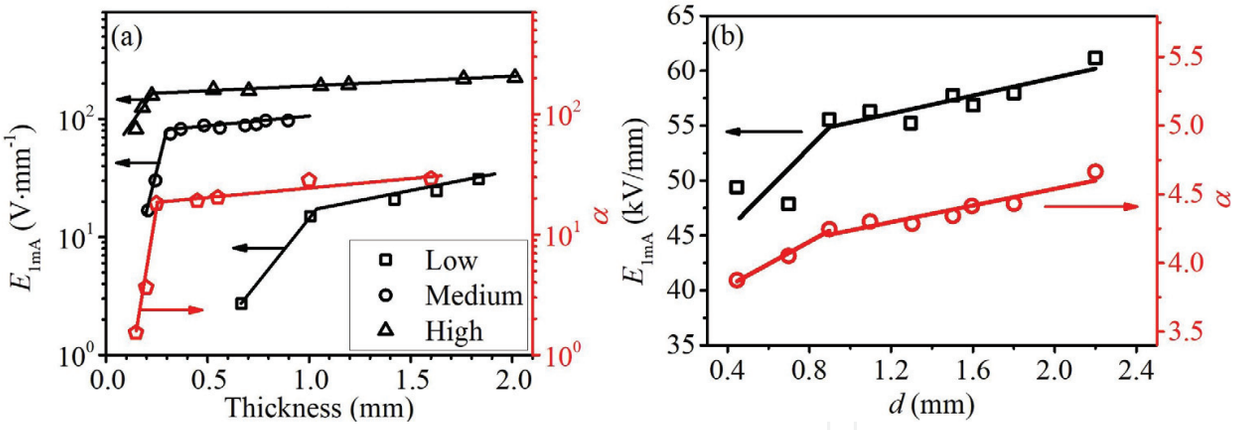

Figure 13. Thickness dependence of E_{1mA} and α of (a) ZnO ceramics and (b) CCTO ceramics.

Samples		b_1	b_2	d_c (mm)	E_c (V/mm)
ZnO ceramics	High	9.4	0.21	0.19	185
	Medium	18.6	0.31	0.28	110
	Low	6.0	0.36	0.98	33
$CaCu_3Ti_4O_{12}$ ceramics		0.278	0.087	0.90	53

Table 7. The exponents b_1 and b_2, critical thickness d_c, and the transitional breakdown field E_c of ZnO ceramics and CCTO ceramics in **Figure 12**.

increased E_{1mA}, suggesting more stable E_{1mA} with variation of thickness. However, no matter what varistors are used in high-voltage or low-voltage situations, dimensional effect undoubtedly exists, which brings much trouble for practical application and design. Therefore, further investigation of dimensional effect is needed for stable electrical performance.

3.2. Simulation of dimensional effect

Breakdown voltage of single grain boundary is acknowledged to be nearly constant (~3 V), indicating other factors should be responsible for dimensional effect. To understand the structural origin of dimensional effect, a model based on the network of grains and grain boundaries is proposed. Grain sizes in varistor ceramics fit the normal distribution, in which the probability density $f(l)$ can be expressed as:

$$f(l) = \frac{1}{\sqrt{2\pi}\sigma} \exp\left[-\frac{(l-\mu)^2}{2\sigma^2}\right], \tag{12}$$

where l is the average grain size, σ is the standard deviation, and μ is the mathematical expectation. For ceramics with diameter of D and thickness of d, it is assumed that all grains are cubic with length of m; the number of grains on the cross-section N is thus calculated as:

$$N = \frac{\pi D^2}{4\mu^2}. \tag{13}$$

It is assumed that these N grains on the cross section lead to N grain chains along thickness direction. Since l also fits normal distribution, the average grain number should be d/m, and the variance of the average grain size should be $\sigma^2/(d/m)$; therefore:

$$f(\bar{l}) = \frac{1}{\sqrt{2\pi}\frac{\sigma}{\sqrt{d/\mu}}} \exp\left[-\frac{(\bar{l}-\mu)^2}{2\frac{\sigma^2}{d/\mu}}\right]. \tag{14}$$

The amount of chains with grain sizes from $\bar{l}$ to $\bar{l} + \Delta\bar{l}$ fits:

$$\Delta n(\bar{l}) = Nf(\bar{l})\Delta\bar{l}, \tag{15}$$

Another assumption is that the current that went through one grain chain is independent on other chains. On this basis, the relationship between the voltage and the current in one grain chain can be expressed as:

$$V = \frac{d}{\bar{l}}V_B + I_i(\bar{l})\frac{d}{\Delta n(\bar{l})\mu^2}\rho_g, \tag{16}$$

where V_B is the breakdown voltage of single grain boundary and ρ_g is the electrical resistivity of grain. Consequently, the total current in this piece of ceramics should be the sum of current flowing in N grain chains:

$$I = \sum I_i(\bar{l}). \tag{17}$$

Based on the model above, *J-E* characteristic under a fixed thickness can be acquired with increased applied voltage V, and the E_{1mA} is able to be calculated. With variance of d in Eq. (12), a series of *J-E* curves are acquired, and E_{1mA} corresponding to different thicknesses are therefore known. According to grain size distribution of the measured ZnO varistor samples with high and medium E_{1mA} found in **Figure 13(a)**, average grain size m and variance σ^2 are calculated and taken into the model. Hence, the thickness dependences of E_{1mA} are plotted in **Figure 14**. The d_c of high-voltage varistors is ~0.2 mm, whereas it is ~0.3 mm for medium-voltage varistors. Both d_c and E_c from simulation fit the experimental results in **Figure 13(a)** well, proving the effectiveness of the proposed model.

In addition, if the average grain size is fixed, sample thickness d is reversely proportional to the variance of the average grain size. The maximum of the probability density $f(\mu)$ fits:

$$f(\mu) = \frac{1}{\sqrt{2\pi}\frac{\sigma}{\sqrt{d/\mu}}}. \tag{18}$$

With increased d, $f(m)$ increases, indicating a narrower grain size distribution. Therefore, dimensional effect of varistor ceramics originated from the thickness dependence of grain size variance.

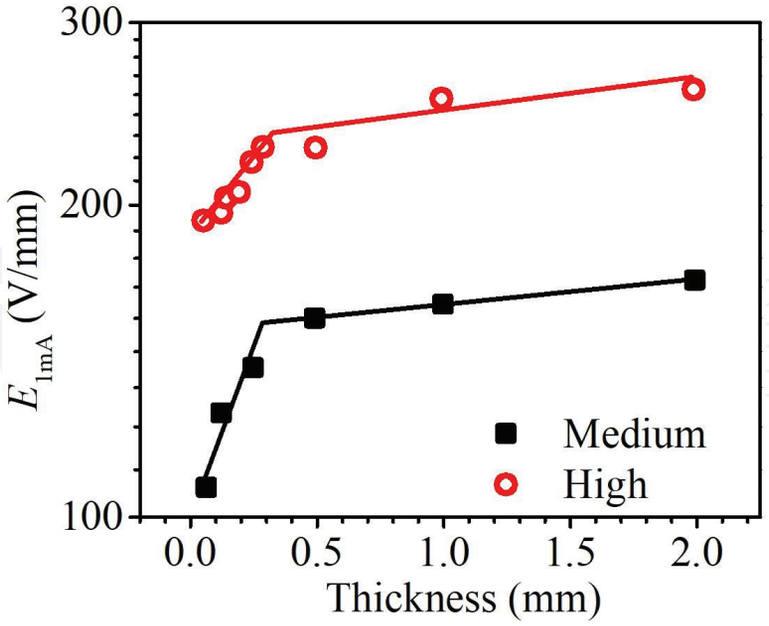

Figure 14. The thickness dependence of breakdown field via simulation (usage permitted by Elsevier).

As for CCTO ceramics which also exhibits dimensional effect shown in **Figure 13(b)**, SEM images and grain size distribution on longitudinal section morphologies are investigated, as shown in **Figure 15**. Grains are smaller near the surface, whereas they are larger and denser in the interior. Quantitative analysis shows that grain sizes are more uniform near the surface while the size distribution is wider in the interior. The average grain size increased from 20.23 μm near the surface to 23.94 μm in the interior, while the porosity decreased from 4.95% near the surface to 0.33% in the interior. Although the grains with size below 30 μm are dominant in number, they contribute less to the section area. It can be seen in **Figure 15(b)**, **(d)**, and **(f)** that although grains with size below 15 μm contribute to more than 50% of grains, the sum of their occupied area is less than 10%. Despite small increase of average grain size from the surface to interior part, the major grain size that contributed to section areas is significantly different. On the surface, amount of the grains between 20 and 40 μm is most, while grains between 40 and 60 μm dominate the section area. Especially, the grain size range extends to 50–90 μm in the interior. From this point, it can be deduced that nonuniform distribution of grain size indeed contributed to dimensional effect in varistor ceramics, which is in accordance with simulation discussed above.

3.3. Elimination of dimensional effect

In not only ZnO varistor ceramics but also CCTO ceramics, dimensional effect exists because of nonuniform grain size distribution, which restricts its practical application. Therefore, in order to diminish or to attenuate dimensional effect, it is important to make grain size distribution more uniform. Despite the traditional processed ZnO varistor ceramics (Tr), another amine processed (Am) samples are prepared. At first, ZnO is dissolved in $NH_4(OH)$ and $NH_4(HCO_3)$

http://dx.doi.org/10.5772/intechopen.79720

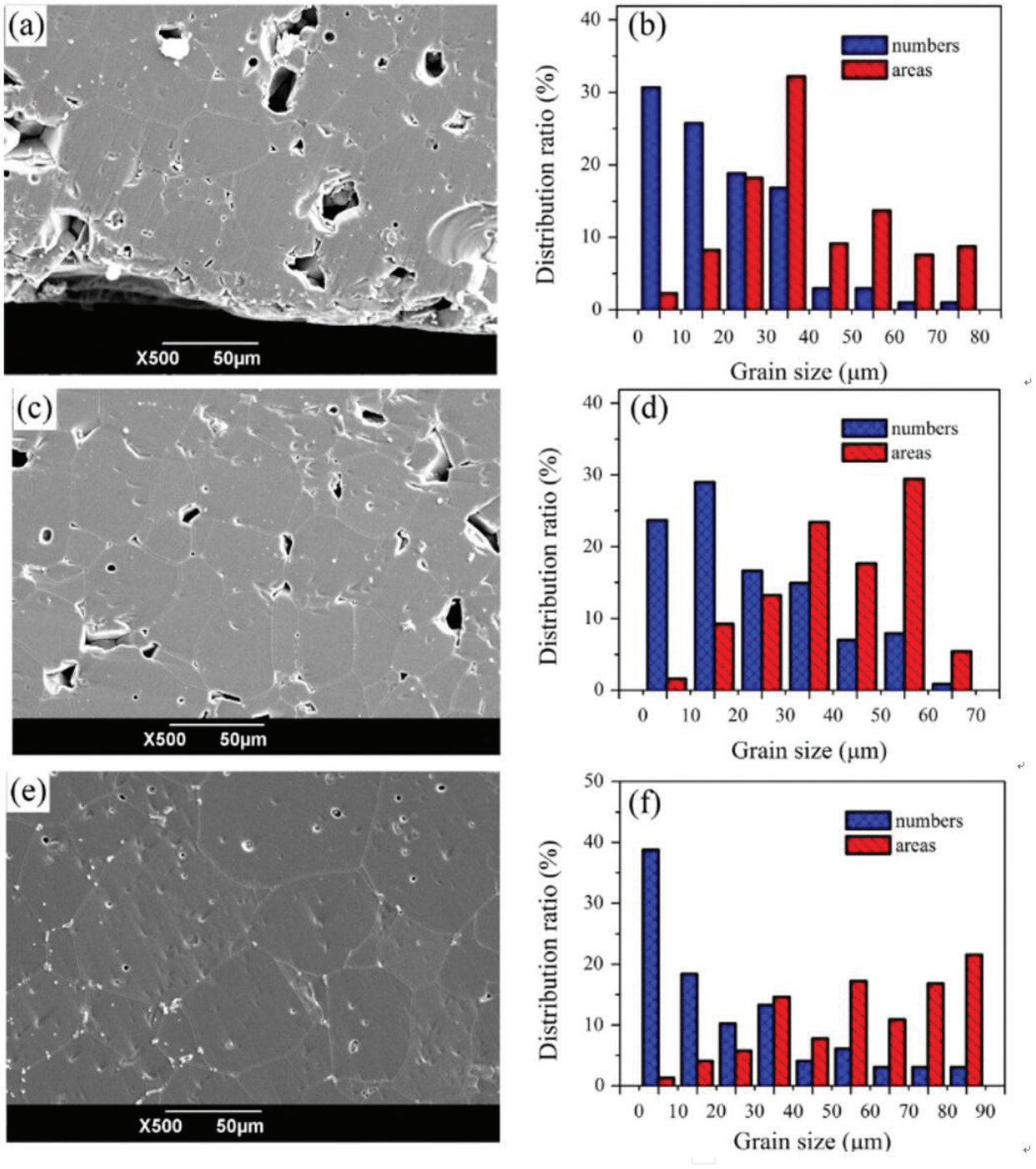

Figure 15. SEM of cross-section morphologies, grain area, and grain size distribution at the surface (a and b), near the surface (c and d), and in the interior (e and f) of CCTO ceramics (usage permitted by Elsevier).

solution with other additives in solutions, which is consequently heated to 110°C. After careful monitoring and controlling the pH of this mixed solution to 8–9, the precipitations are separated from the solution by filtration and washed with diethylamine solution to remove all chloride ions. When the solution is dried, the remained powders are calcined at 500°C, and then traditional processes are followed.

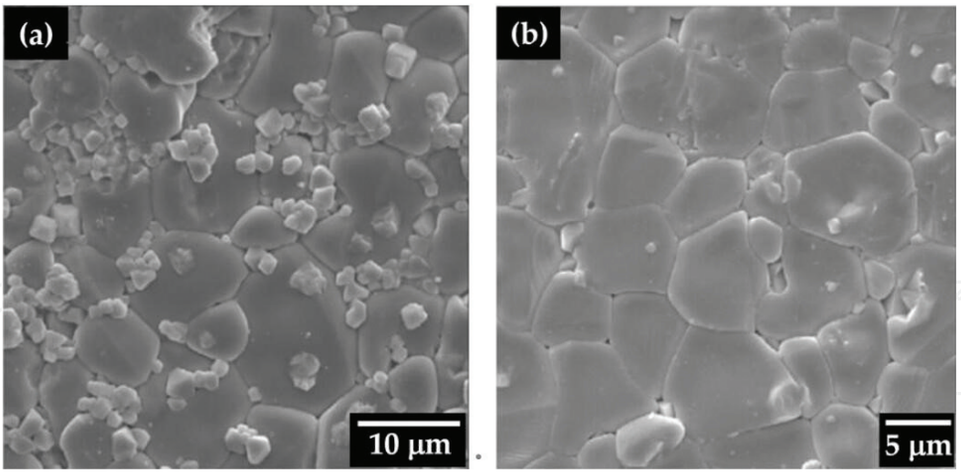

Figure 16. SEM pictures for (a) traditional processed and (b) amine processed ZnO varistors (usage permitted by Elsevier).

SEM photos of traditional processed (Tr) and amine processed (Am) ZnO samples are shown in **Figure 16(a)** and **(b)**, respectively. Lots of small grains are scattered between compactly aligned big grains in Tr samples, as shown in **Figure 16(a)**. However, no such small grains are seen in Am samples. The grains in Am samples are more uniform than those in Tr samples. Lots of grains with size below 3 µm exist in Tr samples, while the grains are compact with almost no grains with size below 3 µm.

Thickness dependence of E_{1mA} of Tr and Am samples are depicted in **Figure 17**. Tr samples exhibit distinct dimensional effect with d_c of 0.28 mm. Notably, the Am samples show lower

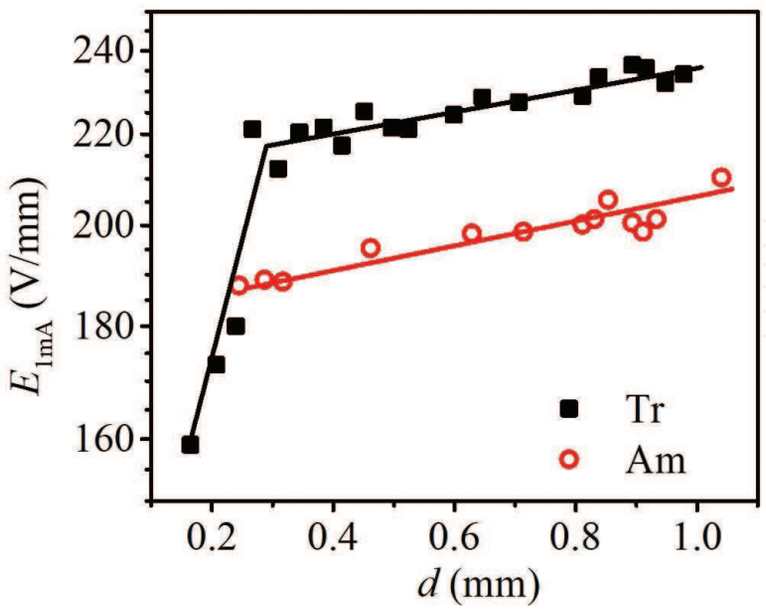

Figure 17. Thickness dependence of E_{1mA} for traditional processed (Tr) ZnO varistors and amine processed (Am) ZnO varistors with identical recipe and processing variables (usage permitted by Elsevier).

E_{1mA} but exhibit no distinct dimensional effect. The decreased E_{1mA} might be attributed to larger average grain size in Am samples than that in Tr samples. What is evident is that uniform grain sizes are obtained, which could effectively eliminate dimensional effect.

4. Conclusion

Breakdown characteristics in varistor ceramics are investigated from grain boundary characteristics based on single barrier performance and barrier distribution. On one hand, different methods of doping including substitution and additional phase result in not only restriction on grain sizes but also manipulation of defects in Schottky barriers of varistor ceramics to enhance breakdown field to meet the requirement of device miniaturization. In addition, restriction on further decreased thickness of varistor ceramics is found as dimensional effect in not only ZnO ceramics but also $CaCu_3Ti_4O_{12}$ ceramics. From theoretical analysis and experimental results, the dimensional effect is found closely related with the uniformity of grain sizes, which influence the distribution of grain boundaries quite well. Consequently, the breakdown characteristics in varistor ceramics are understood from the aspect of single barrier performance and spatial distribution of barriers.

Author details

Jianying Li*, Kangning Wu and Yuwei Huang

*Address all correspondence to: lijy@xjtu.edu.cn

State Key Laboratory of Electrical Insulation and Power Equipment, Xi'an Jiaotong University, Xi'an, China

References

[1] Matsuoka M. Nonohmic properties of zinc oxide ceramics. Japanese Journal of Applied Physics. 1971;**10**:736-746. DOI: 10.1143/JJAP.10.736

[2] Sinclair DC, Adams TB, Morrison FD, West AR. $CaCu_3Ti_4O_{12}$: One-step internal barrier layer capacitor. Applied Physics Letters. 2002;**80**:2153-2155. DOI: 10.1063/1.1463211

[3] Chung SY, Kim ID, Kang SJ. Strong nonlinear current-voltage behaviour in perovskite-derivative calcium copper titanate. Nature Materials. 2004;**3**:774-778. DOI: 10.1038/nmat1238

[4] Blatter G, Greuter F. Carrier transport through grain boundaries in semiconductors. Physical Review B. 1986;**33**:3952-3966. DOI: 10.1103/PhysRevB.33.3952

[5] Tang Z, Huang Y, Wu K, Li J. Significantly enhanced breakdown field in $Ca_{1-x}Sr_xCu_3Ti_4O_{12}$ ceramics by tailoring donor densities. Journal of the European Ceramic Society. 2018;**38**:1569-1575. DOI: 10.1016/j.jeurceramsoc.2017.11.018

[6] Li J, Jia R, Tang X, Zhao X, Li S. Enhanced electric breakdown field of $CaCu_3Ti_4O_{12}$ ceramics: Tuning of grain boundary by a secondary phase. Journal of Physics D: Applied Physics. 2013;**46**:325304. DOI: 10.1088/0022-3727/46/32/325304

[7] Jia R, Zhao X, Li J, Tang X. Colossal breakdown electric field and dielectric response of Al-doped $CaCu_3Ti_4O_{12}$ ceramics. Materials Science and Engineering: B. 2014;**185**:79-85. DOI: 10.1016/j.mseb.2014.02.015

[8] Li J, Hou L, Jia R, Gao L, Wu K, Li S. Influences of $CuAl_2O_4$ doping on the dielectric properties of $CaCu_3Ti_4O_{12}$ ceramics. Journal of Materials Science: Materials in Electronics. 2015;**26**:5085-5091. DOI: 10.1007/s10854-015-3033-0

[9] Li J, Wu K, Jia R, Hou L, Gao L, Li S. Towards enhanced varistor property and lower dielectric loss of $CaCu_3Ti_4O_{12}$ based ceramics. Materials & Design. 2016;**92**:546-551. DOI: 10.1016/j.matdes.2015.12.073

[10] Tang Z, Wu K, Huang Y, Li J. High breakdown field $CaCu_3Ti_4O_{12}$ ceramics: Roles of the secondary phase and of Sr doping. Energies. 2017;**10**:1031. DOI: 10.3390/en10071031

[11] Chaim R, Chevallier G, Weibel A, Estournes C. Grain growth during spark plasma and flash sintering of ceramic nanoparticles: A review. Journal of Materials Science. 2018;**53**: 3087-3105. DOI: 10.1007/s10853-017-1761-7

[12] Pourrahimi AM, Liu D, Strom V, Hedenqvist MS, Olsson RT, Gedde UW. Heat treatment of ZnO nanoparticles: New methods to achieve high-purity nanoparticles for high-voltage applications. Journal of Materials Chemistry A. 2015;**3**:17190-17200

[13] Eda K. Destruction mechanism of zno varistors due to high currents. Journal of Applied Physics. 1984;**56**:2948-2955. DOI: 10.1063/1.333836

[14] Smeets R, van der Linden WA. Verification of the short-circuit current making capability of high-voltage switching devices. IEEE Transactions on Power Delivery. 2001;**16**:611-618. DOI: 10.1109/61.956746

[15] Li J, Li B, Zhai D, Li S, Alim MA. Dielectric response on the critical breakdown field in ZnO varistors. Journal of Physics D-Applied Physics. 2006;**39**:4969-4974. DOI: 10.1088/0022-3727/39/23/011

[16] Li J, Jia R, Hou L, Gao L, Wu K, Li S. The dimensional effect of dielectric performance in $CaCu_3Ti_4O_{12}$ ceramics: Role of grain boundary. Journal of Alloys and Compounds. 2015; **644**:824-829. DOI: 10.1016/j.jallcom.2015.05.095

[17] Li ST, Li JY, Alim MA. Structural origin of dimensional effect in ZnO varistors. Journal of Electroceramics. 2003;**11**:119-124. DOI: 10.1023/B:JECR.0000015668.26785.89

[18] Hohenberger G, Tomandl G, Ebert R, Taube T. Inhomogeneous conductivity in varistor ceramics: Methods of investigation. Journal of the American Ceramic Society. 2010;**74**: 2067-2072. DOI: 10.1111/j.1151-2916.1991.tb08260.x

[19] Greuter F, Blatter G. Electrical-properties of grain-boundaries in polycrystalline compound semiconductors. Semiconductor Science and Technology. 1990;**5**:111-137. DOI: 10.1088/0268-1242/5/2/001

[20] Adams TB, Sinclair DC, West AR. Giant barrier layer capacitance effects in $CaCu_3Ti4O_{12}$ ceramics. Advanced Materials. 2002;**14**:1321. DOI: 10.1002/chin.200251017

[21] Mukae K, Tsuda K, Nagasawa I. Capacitance-vs-voltage characteristics of ZnO varistors. Journal of Applied Physics. 1979;**50**:4475. DOI: 10.1063/1.326411

[22] Li J, Subramanian MA, Rosenfeld HD, Jones CY, Toby BH, Sleight AW. Clues to the giant dielectric constant of $CaCu_3Ti_4O_{12}$ in the defect structure of "$SrCu_3Ti_4O_{12}$". Chemistry of Materials. 2004;**16**:5223-5225. DOI: 10.1021/cm048345u

[23] Schmidt R, Pandey S, Fiorenzad P, Sinclairb DC. Non-stoichiometry in "$CaCu_3Ti_4O_{12}$" (CCTO) ceramics. RSC Advances. 2013;**3**:14580-14589. DOI: 10.1039/C3RA41319E

[24] Ramírez MA, Bueno PR, Varela JA, Longo E. Non-Ohmic and dielectric properties of a $Ca_2Cu_2Ti_4O_{12}$ polycrystalline system. Applied Physics Letters. 2006;**89**:212102. DOI: 10.1063/1.2393122

[25] Ribeiro WC, Araujo RGC, Bueno PR. The dielectric suppress and the control of semiconductor non-Ohmic feature of $CaCu_3Ti_4O_{12}$ by means of tin doping. Applied Physics Letters. 2011;**98**:323. DOI: 10.1063/1.3574016

[26] Thongbai P, Boonlakhorn J, Putasaeng B, Yamwong T, Maensiri S. Extremely enhanced nonlinear current-voltage properties of Tb-doped $CaCu_3Ti_4O_{12}$ ceramics. Journal of the American Ceramic Society. 2013;**96**:379-381. DOI: 10.1111/jace.12157

IntechOpen